Materials International
Open Access Journal (ISSN: 2668-5728)

Article
Volume 7, Issue 1, 2025, 3
https://doi.org/10.33263/Materials71.003

Design, Functionalization, and Characterization of InGaN Nanocluster for Energy Storage in Solar Cell Basics: A Quantum Chemistry Study

Fatemeh Mollaamin [1,*]

[1] Department of Biomedical Engineering, Faculty of Engineering and Architecture, Kastamonu University, Kastamonu, Turkey
* Correspondence: fmollaamin@kastamonu.edu.tr ; smollaamin@gmail.com (F.M.)
Scopus Author ID: 35848813100

Received: 20.08.2024; Accepted: 06.10.2024; Published: 6.01.2025

Abstract: A comprehensive investigation on energy grabbing by Ga_8N_9, In_8N_9, $In_4Ga_4N_9$, Si–$In_3Ga_4N_9$, Zn–$In_3Ga_4N_9$, Ag–$In_3Ga_4N_9$ was carried out, including using DFT computations at the CAM–B3LYP–D3/6-311+G (d,p) level of theory. The hypothesis of the energy adsorption phenomenon was confirmed by density distributions of CDD, TDOS, and ELF for Ga_8N_9, In_8N_9, $In_4Ga_4N_9$, Si–$In_3Ga_4N_9$, Zn–$In_3Ga_4N_9$, Ag–$In_3Ga_4N_9$ hetero-clusters. Therefore, it can be considered that zinc and silver atoms in the functionalized Zn–$In_3Ga_4N_9$ and Ag–$In_3Ga_4N_9$ may have more effective sensitivity for admitting the electrons in the status of energy adsorption mechanism. Furthermore, Ag–In3Ga4N9 is potentially advantageous for certain high-frequency applications requiring solar cells for energy saving.

Keywords: solar cells; energy storage; $In_4Ga_4N_9$; Si–$In_3Ga_4N_9$; Zn–$In_3Ga_4N_9$; Ag–$In_3Ga_4N_9$; DFT.

1. Introduction

The nitrides of group III in the periodic table have low sensitivity to ionizing radiation, which makes them appropriate materials for solar cell arrays for satellites. Therefore, space applications could benefit as devices have shown stability in high radiation environments. Because GaN transistors can operate at much higher temperatures and work at much higher voltages than gallium arsenide (GaAs) transistors, they make ideal power amplifiers at microwave frequencies. In addition, GaN offers promising characteristics for THz devices. Due to high power density and voltage breakdown limits, GaN is also emerging as a promising candidate for 5G cellular base station applications [1–3].

GaN with a high crystalline quality can be obtained by depositing a buffer layer at low temperatures [4]. Such high-quality GaN led to the discovery of p-type GaN [5], p–n junction blue/UV-LEDs [5], and room-temperature stimulated emission [6]. This has led to the commercialization of high-performance blue LEDs and long-lifetime violet laser diodes and the development of nitride-based devices such as UV detectors and high-speed field-effect transistors [7].

GaN-based metal–oxide semiconductor field-effect transistor (MOSFET) and metal-semiconductor field-effect transistor (MESFET) transistors also offer advantages, including a lower loss in high-power electronics, especially in automotive and electric car applications [8].

The U.S. Army Research Laboratory (ARL) first measured the high field electron velocity in GaN in 1999 [9]. Scientists at ARL experimentally obtained a peak steady-state velocity of 1.9×10^7 cm/s, with a transit time of 2.5 picoseconds, attained at an electric field of 225 kV/cm. With this information, the electron mobility was calculated, thus providing data for the design of GaN devices.

The ternary semiconductor of Indium gallium nitride (InGaN) as solar cells is remarkable owing to the adjustable direct band gap energy of InGaN, veiling the total solar spectrum arraying from 0.7 to 3.4 eV [10,11], as well as preferable photovoltaic specifics of InGaN consisting of vast absorption coefficients [12] and high carrier dynamism. Furthermore, InGaN alloys' great fixity and excellent radiation persistence permit the function of InGaN-based instruments in uttermost situations such as space and geocentric usages [10,13]. The solar cells of InGaN were constructed with low indium amounts of the InGaN alloy compounds [14–16], which conduces to an enhancement in the band gap energy of InGaN and then eventuates in the absorption of shorter wavelengths of solar radiation. Therefore, to find out InGaN solar cells with high yield, the amount in the InGaN active layer of these solar cells should be enhanced to compensate for a large part of the solar spectrum. Recently, it has been suggested that dual nano gratings of Si and other organic solar cells be applied, which are mostly in direct contact with the active area of the solar cells [17–23].

Moreover, the researchers fabricated transition metal zinc doped InGaN nanorods arrays by radio-frequency plasma-assisted molecular beam epitaxy. Doping reduces the composition of indium atoms and the aggregation of In–In and induces deep energy levels. This greatly decreases the defects and improves the valence band potential of InGaN nanorods [24].

Recently, researchers have proposed an InGaN/GaN p-i-n thin-film solar cell, which includes a dual nanograting compound: silver nano gratings on the back of the solar cell and GaN-NGs on the front. FDTD simulation parameters have exhibited that the dual NG compound connects the eventual sunlight to the plasmonic and photonic styles, enhancing the solar cell's absorption in a wide spectral span. It is perceived that the solar cells possessing the double nanograting structures have a considerable increment in light absorption compared with cells having either no nanogratings or only the front nanogratings or the back nanogratings [25].

In this paper, we propose a feasible ternary semiconductor of an Indium Gallium Nitride solar cell doped with silicon, zinc, or silver. We carried out molecular modeling considering the geometrical parameters of doping atoms on the surface of $In_4Ga_4N_9$ through the solar cells' absorption status and current charge density. Moreover, the effect of a relative chemical shift between $In_4Ga_4N_9$ and doped hetero-clusters of the solar cell was also studied.

2. Materials and Methods

In this work, the Si-, Zn-, or Ag-doped $In_4Ga_4N_9$ solar cells were calculated within the framework of first-principle calculation based on density functional theory (DFT) (Figure 1). The rigid potential energy surface using density functional theory [26– 39] was performed due to the Gaussian 16 revision C.01 program package [40] and GaussView 6.1 [41]. The coordination input for energy storage on the solar cells has applied 6-311+G (d,p) and EPR–3 basis sets.

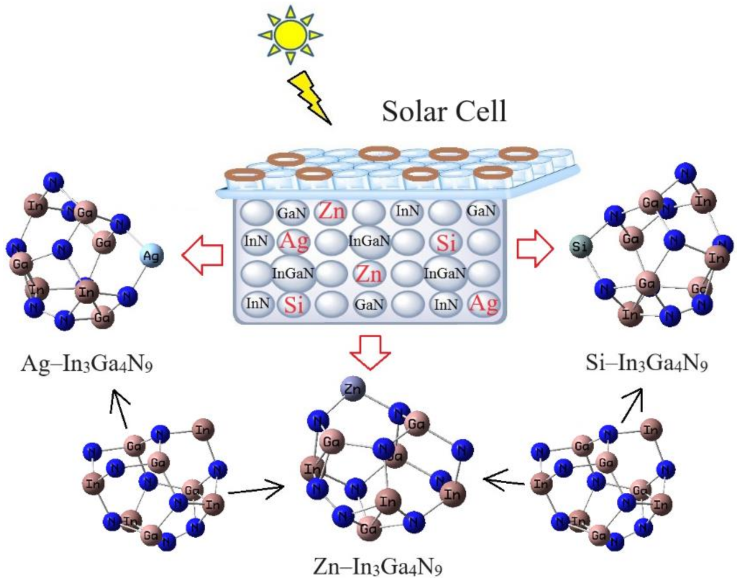

Figure 1. Application of hetero-clusters of Ga_8N_9, In_8N_9, $In_4Ga_4N_9$, Si–$In_3Ga_4N_9$, Zn–$In_3Ga_4N_9$ and Ag–$In_3Ga_4N_9$ for energy storage in solar cells using CAM–B3LYP–D3/6-311+G (d,p) calculation.

Figure 1 has shown the process of energy storage on hetero-clusters of Ga_8N_9, In_8N_9, $In_4Ga_4N_9$, Si–$In_3Ga_4N_9$, Zn–$In_3Ga_4N_9$, and Ag–$In_3Ga_4N_9$, which is modified to enlarge the absorption in the active zone. Further, we optimized the structural parameters of nanocages of Ga_8N_9, In_8N_9, a ternary semiconductor of $In_4Ga_4N_9$solar cell which is doped with silicon, zinc or silver towards formation of hetero-clusters of Si–$In_3Ga_4N_9$, Zn–$In_3Ga_4N_9$, Ag–$In_3Ga_4N_9$ for obtaining the greatest short current aggregate in these solar cell structures.

3. Results and Discussion

3.1. CDD, TDOS, and ELF analysis.

The amounts of charge density differences "CDD" are measured by considering isolated atoms or noninteracting ones. The mentioned approximation can be the lightest to use because the superposition value may be received from the primary status of the self-consistency cycle in the code that carries out the density functional theory (Figures 2a–f) [42].

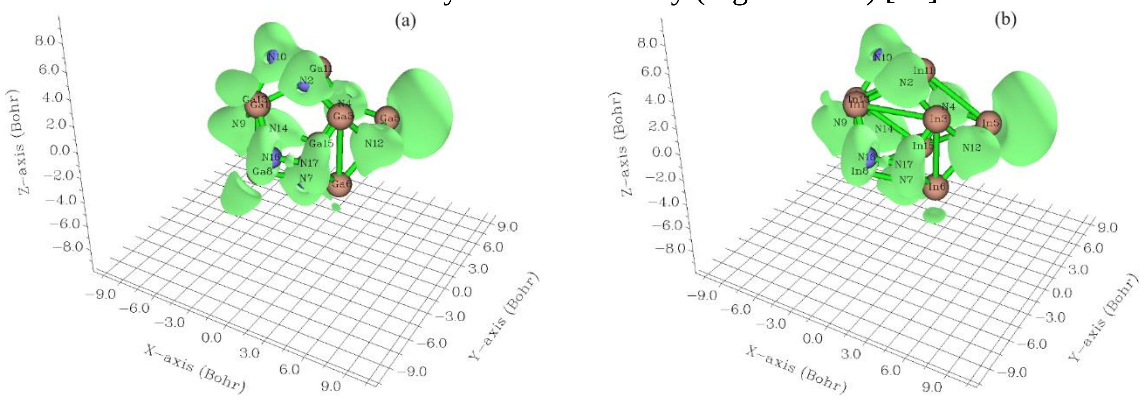

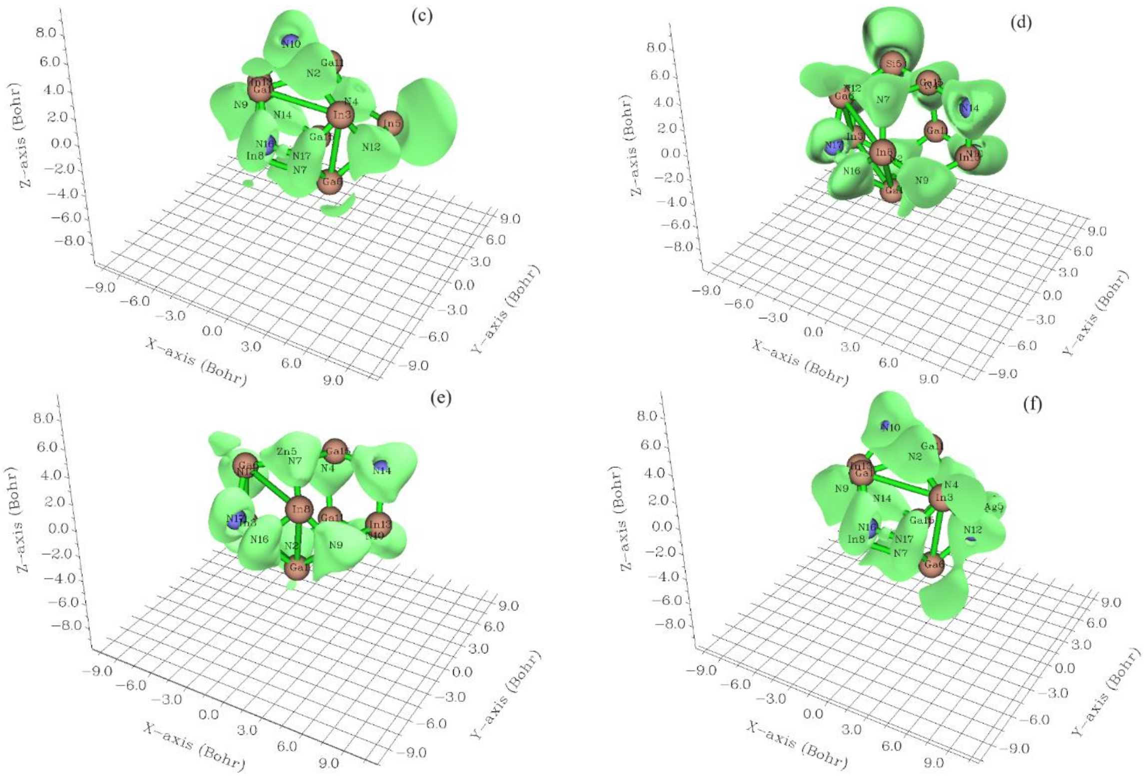

Figure2. CDD graphs for hetero-clusters of **(a)** Ga_8N_9; **(b)** In_8N_9; **(c)** $In_4Ga_4N_9$; **(d)** Si–$In_3Ga_4N_9$; **(e)** Zn–$In_3Ga_4N_9$; **(f)** Ag–$In_3Ga_4N_9$.

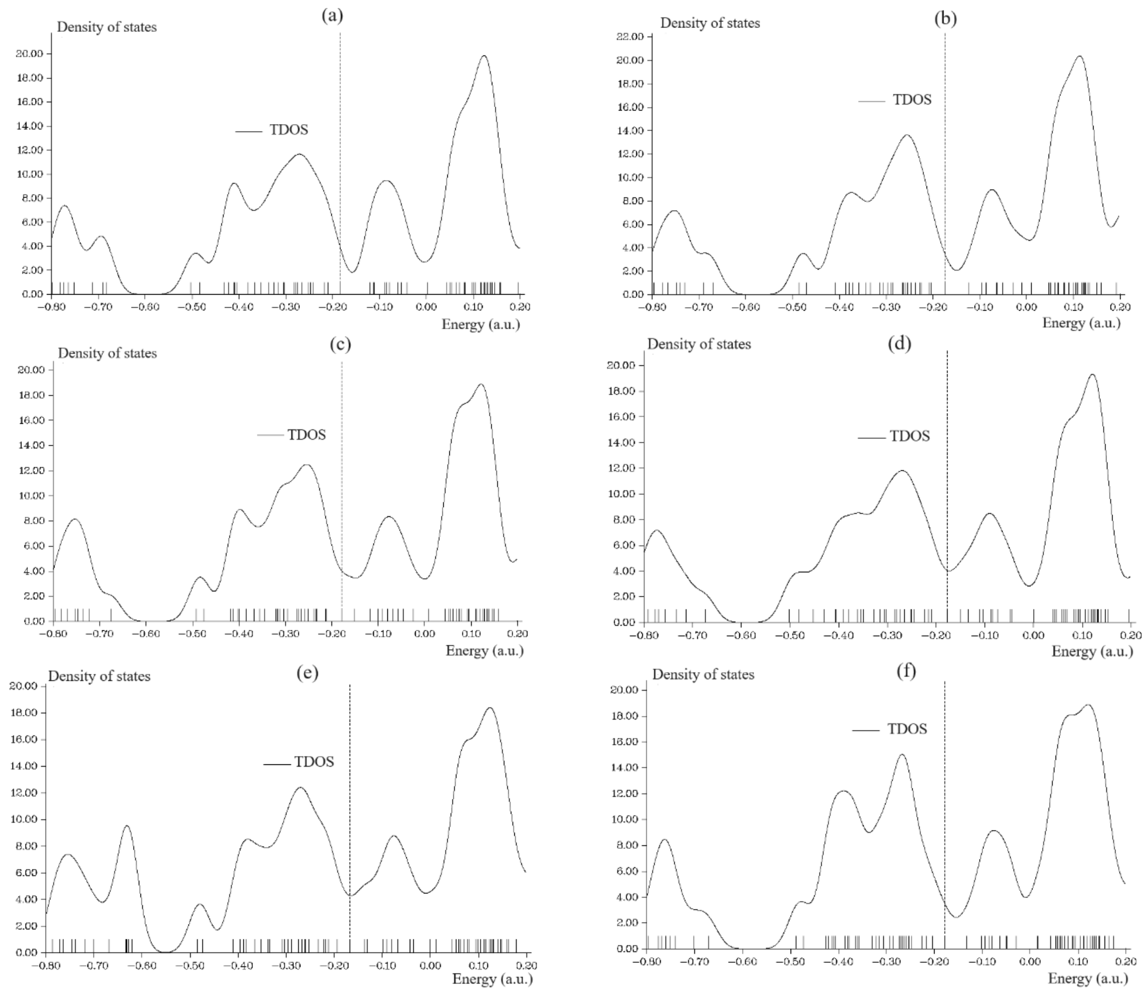

Figure 3. TDOS graphs of hetero-clusters include **(a)** Ga_8N_9; **(b)** In_8N_9; **(c)** $In_4Ga_4N_9$; **(d)** Si–$In_3Ga_4N_9$; **(e)** Zn–$In_3Ga_4N_9$; **(f)** Ag–$In_3Ga_4N_9$.

In Figure 2a, the atoms of N(10), N(12), N(14), N(16), N(17) from Ga_8N_9 have shown a fluctuation around –9 to +4.5 Bohr. The atoms of N(10), N(14), N(16), N(17) from In_8N_9 have indicated the fluctuation around –9 to + 5 Bohr (Figure 2b). In Figure 2c, N(10) and N(14) atoms extracted from the ternary hereto-cluster of $In_4Ga_4N_9$ have exhibited a fluctuation around –9 to + 5.5 Bohr. Then, the two doped hereto-clusters of Si–$In_3Ga_4N_9$ (Figure 2d) and Zn–$In_3Ga_4N_9$ (Figure 2e) with active atoms of N(10), N(14), N(16), N(17) have been oscillated around –9 to + 2.5 Bohr. However, in the doped hereto-cluster of Ag–$In_3Ga_4N_9$, except for atoms of N(10), N(14), N(16), and N(17), the Ag (5) has been considered as a fluctuated atom around –9 to + 3 Bohr (Figure 2f).

Squirming the molecular orbital data owing to Gaussian graphs of unit altitude and entire width at half maximum (FWHM) of 0.3 eV by GaussSum 3.0.2 [43] have computed the total density of states (TDOS). To further realize the different adsorption specifications by Ga_8N_9, In_8N_9, $In_4Ga_4N_9$, Si–$In_3Ga_4N_9$, Zn–$In_3Ga_4N_9$, Ag–$In_3Ga_4N_9$, TDOS has been measured. This parameter can indicate the existence of important chemical interactions often on the convex side (Figures 3a–f).

The maximum energy of TDOS for Ga_8N_9 (Figure 3a) and In_8N_9 (Figure 3b) has a sharp peak of around –0.3 a.u. Figure 3c shows the ternary semiconductor of $In_4Ga_4N_9$ with a sharp peak around –0.3 a.u. and a weak peak around –0.4 a.u. After doping Si on $In_4Ga_4N_9$ hetero-cluster, the peak around –0.4 a.u. has been more clarified (Figure 3d). It is remarkable that the excessive growth technique on doping silicon is a potential approach to designing high-efficiency semipolar gallium nitride devices on silicon layers in a long wavelength zone. Moreover, similar amounts of TDOS were found for Zn–In3Ga4N9, with a sharper peak of around –0.4 a.u. than Si–$In_3Ga_4N_9$ makes $In_4Ga_4N_9$ a more effective solar cell for adsorption energy (Figure 3e). However, Ag–$In_3Ga_4N_9$ has shown three notable peaks around –0.28, –0.4, and –0.8 a.u. can be more efficient than $In_4Ga_4N_9$ (Figure 3f).

Furthermore, a type of scalar field called electron localization function “ELF” may demonstrate a broad span of bonding samples. Nevertheless, the distinction between deduced/raised electron delocalization/localization into cyclic π-conjugated sets stays encouraging for “ELF” [44]. The grosser the electron localization is in an area, the more likely the electron movement is restricted. Therefore, they might be discerned from the ones away if electrons are centralized. As Bader investigated, the zones with large electron localization possess extensive magnitudes of Fermi hole integration. However, with a six-dimensional function for the Fermi hole, it seems hard to study directly. Then, Becke and Edgecombe remarked that spherically averaged spin conditional pair probability possesses a direct correlation with the Fermi hole and proposed the parameter of electron localization function (ELF) in the Multiwfn program [45] and popularized for the spin-polarized procedure [46]:

$$\mathrm{ELF(r)} = \frac{1}{1+[D(\mathrm{r})/D_0(\mathrm{r})]} \tag{1}$$

Where

$$D(\mathrm{r}) = \frac{1}{2}\sum_i \eta_i \left|\nabla\varphi_i\,(\mathrm{r})\right|^2 - \frac{1}{8}\left[\frac{|\nabla\rho_\alpha\,(\mathrm{r})|^2}{\rho_\alpha\,(\mathrm{r})} + \frac{|\nabla\rho_\beta\,(\mathrm{r})|^2}{\rho_\beta\,(\mathrm{r})}\right] \tag{2}$$

and

$$D_0(\mathrm{r}) = \frac{3}{10}(6\pi^2)^{2/3}\left[\rho_\alpha\,(\mathrm{r})^{5/3} + \rho_\beta\,(\mathrm{r})^{5/3}\right] \tag{3}$$

For close-shell system, since $\rho_\alpha = \rho_\beta = (1/2)\rho$, *D*, and *D*0 terms can be simplified as:

$$D(\mathrm{r}) = \frac{1}{2}\sum_i \eta_i \,|\nabla\varphi_i\,(\mathrm{r})|^2 - \frac{1}{8}\frac{|\nabla\rho\,(\mathrm{r})|^2}{\rho\,(\mathrm{r})} \quad (4)$$

And

$$D_0(\mathrm{r}) = (3/10)(3\pi^2)^{2/3}\,\rho\,(\mathrm{r})^{5/3} \quad (5)$$

Regarding kinetic energy, "ELF" was rechecked to be more punctual for both Kohn-Sham DFT and post-HF wavefunctions [47]. The excess kinetic energy density caused by Pauli repulsion was unfolded by D(r), and D0(r) may be inspected as Thomas-Fermi kinetic energy density. Because D0(r) is brought forward, the ELF is the origin, and the ELF shows an affiliate localization. The compounds of Ga_8N_9, In_8N_9, $In_4Ga_4N_9$, Si–$In_3Ga_4N_9$, Zn–$In_3Ga_4N_9$, and Ag–$In_3Ga_4N_9$ can be defined by ELF graphs owing to exploring their delocalization/localization characterizations of electrons and chemical bonds (Figure 4a–f).

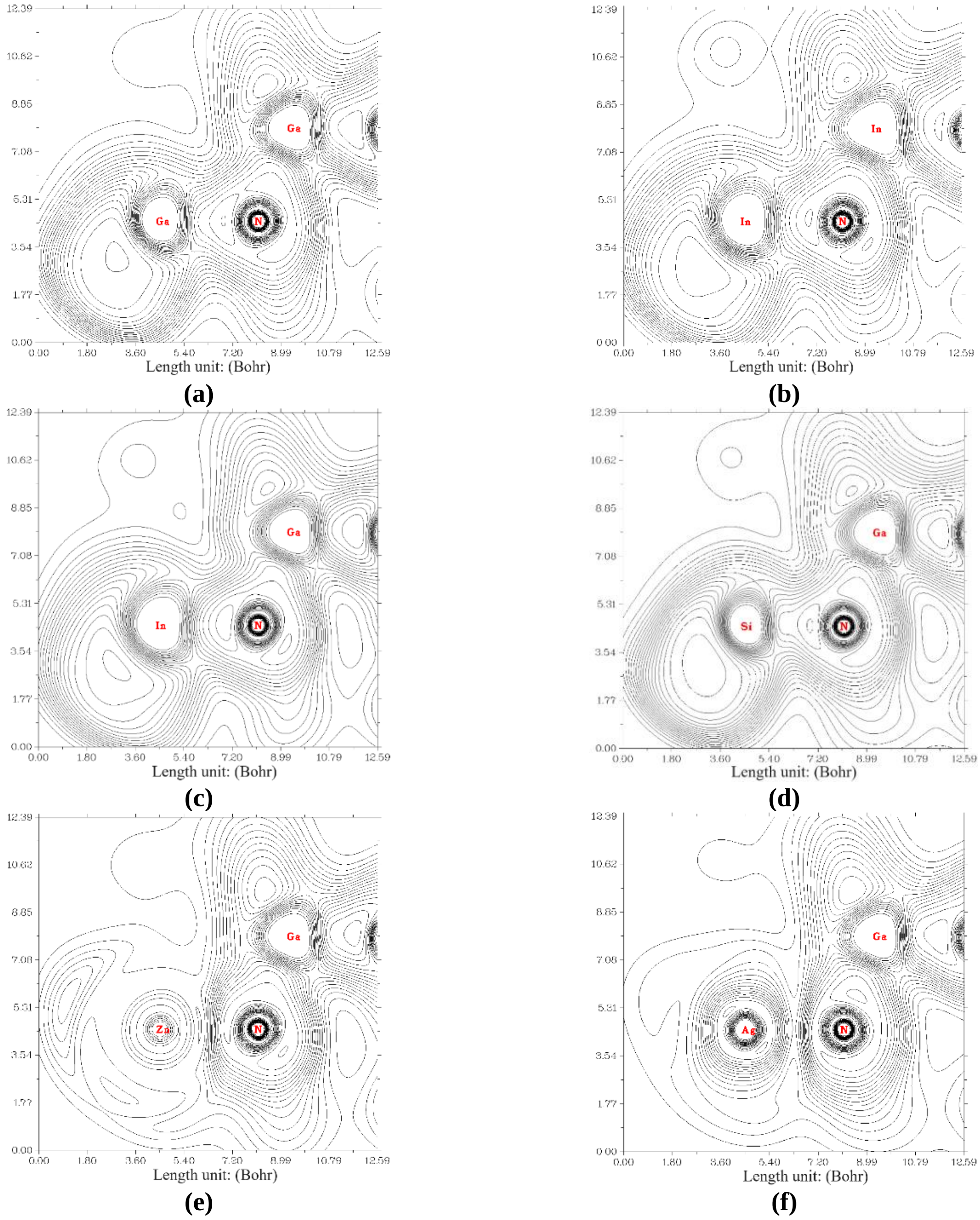

Figure 4. The graphs of ELF for hetero-clusters include **(a)** Ga_8N_9; **(b)** In_8N_9; **(c)** $In_4Ga_4N_9$; **(d)** Si–$In_3Ga_4N_9$; **(e)** Zn–$In_3Ga_4N_9$; **(f)** Ag–$In_3Ga_4N_9$. (Counter line map on the right and shaded surface map with projection on the left).

The counter map of ELF for Ga_8N_9 and In_8N_9 has shown the electron delocalization of these two hetero-clusters based on labeling atoms of N(4), Ga (5), Ga (15) for Ga_8N_9 (Figure 4a) and N(4), In (5), In (15) for In_8N_9 (Figure 4b), respectively. Then, the formation of a ternary alloy of $In_4Ga_4N_9$ indicates an isosurface map of electron delocalization due to labeling atoms of N(4), In (5), Ga (15) (Figure 4c). A vaster jointed area engaged by an isosurface map for Si, Zn, Ag doping $In_4Ga_4N_9$ towards the formation of hetero-clusters of Si–$In_3Ga_4N_9$(Figure 4d), Zn–$In_3Ga_4N_9$ (Figure 4e) and Ag–$In_3Ga_4N_9$ (Figure 4f) due to labeling atoms of N(4), Si/Zn/Ag (5), Ga (15), respectively. A narrower connected area occupied by an isosurface map means that electron delocalization is relatively difficult. However, the large counter map of ELF for Ag–$In_3Ga_4N_9$, Zn–$In_3Ga_4N_9$, and Si–$In_3Ga_4N_9$ hetero-clusters can confirm that doping Ag, Zn, and Si nanoparticles on the surface, respectively, increases the efficiency of the ternary solar cell of $In_3Ga_4N_9$ for energy storage.

Besides, the changes of charge density analysis have illustrated that $In_3Ga_4N_9$ has shown the Bader charge of –1.131 coulomb, and after doping with silicon, zinc and silver has indicated the Bader charge of –1.172, –1.171 and –1.159 coulomb for Si–$In_3Ga_4N_9$, Zn–$In_3Ga_4N_9$, Ag–$In_3Ga_4N_9$, respectively, that describes the tensity value of these hetero-clusters for energy storage.

3.2. Insight of infrared spectroscopy and thermochemistry.

Infrared spectroscopy (IR) has been performed for Ga_8N_9, In_8N_9 nanocages, ternary alloy of $In_3Ga_4N_9$, and doped hetero-clusters of Si–$In_3Ga_4N_9$, Zn–$In_3Ga_4N_9$, Ag–$In_3Ga_4N_9$ (Figure 5a–f). Therefore, it has been simulated the several clusters containing Ga_8N_9 (Figure 5a), In_8N_9 (Figure 5b), $In_3Ga_4N_9$ (Figure 5c), Si–$In_3Ga_4N_9$ (Figure 5d), Zn–$In_3Ga_4N_9$ (Figure 5e), and Ag–$In_3Ga_4N_9$ (Figure 5f).

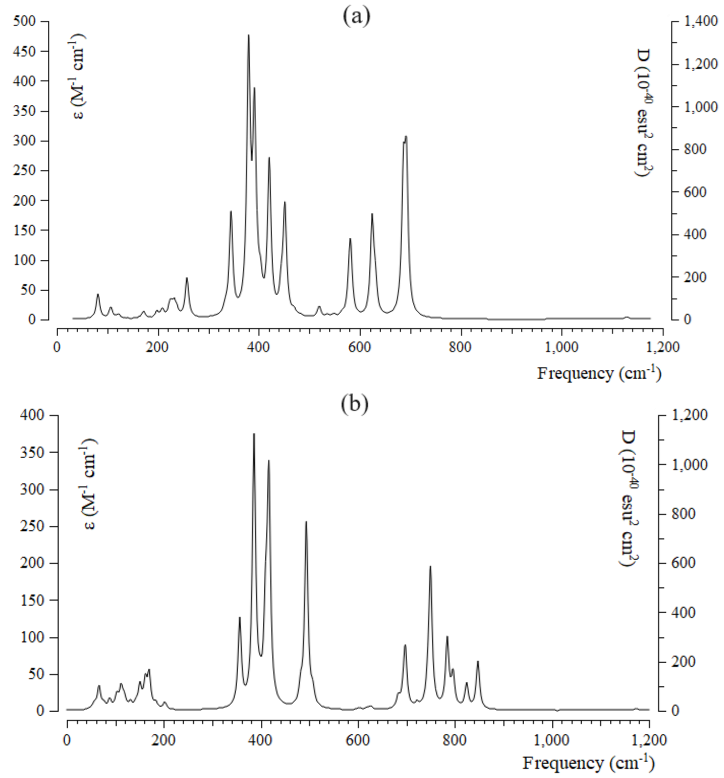

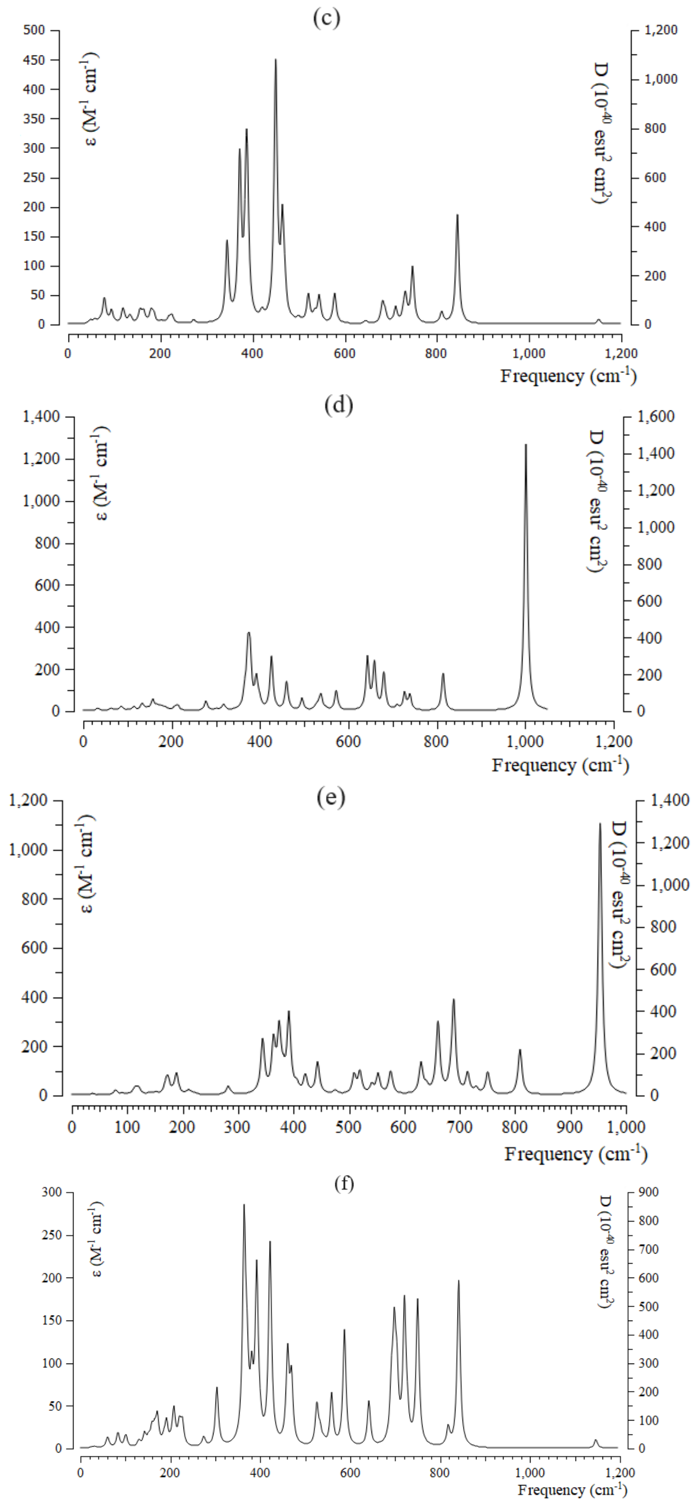

Figure 5. The frequency (cm^{-1}) changes through the IR spectra for hetero-clusters of **(a)** Ga_8N_9; **(b)** In_8N_9; **(c)** $In_4Ga_4N_9$; **(d)** Si–$In_3Ga_4N_9$; **(e)** Zn–$In_3Ga_4N_9$; **(f)** Ag–$In_3Ga_4N_9$.

The frequency values through the IR curves between 100–1200 cm^{-1} have been achieved for Ga_8N_9 with several sharp peaks around 391.27, 420.84, 451.72, 581.93, 624.62, 686.54 and 692.45 cm^{-1} (Figure 5a). Figure 5 (b) shows the frequency range between 100–1200 cm^{-1} for In8N9 with sharp peaks around 356.43, 385.93, 409.88, 416.57, 493.70, and 749.78 cm^{-1}. Figure 5 (c) indicates the frequency fluctuation between 100–1200 cm^{-1} for $In_4Ga_4N_9$ with sharp peaks around 386.14, 388.65, 450.05, 464.72 and 844.38 cm^{-1}. The graph of Figure 5 (d) has been observed in the frequency range between 200–1100 cm^{-1} for Si–In_3Ga_4N9 with several sharp peaks around 372.66, 377.37, 425.97, 643.15, 658.78, 814.28 and 1001.62 cm^{-1}.

Figure 5 (e) shows the frequency range between 100–1100 cm^{-1} for Zn–$In_3Ga_4N_9$ with sharp peaks around 344.39, 363.95, 374.21, 391.72, 443.55, 660.86, 689.18, 808.93 and 953.51 cm^{-1}. Furthermore, the graph of Figure 5(f) has been observed in the frequency range between 100–1200 cm^{-1} for Ag–$In_3Ga_4N_9$ with several sharp peaks around 364.05, 392.08, 421.72, 720.67, 749.85 and 841.15 cm^{-1}.

Energy storage with hetero-clusters has described that the frame of the overcoming cluster is related to Ag–$In_3Ga_4N_9$ in the high amounts of frequency. This property makes Ag–$In_3Ga_4N_9$ potentially advantageous for certain high-frequency applications requiring solar cells for energy storage. The advantages of silver over indium gallium nitride include its higher electron and hole mobility, allowing silver doping devices to operate at higher frequencies than silicon and zinc doping devices.

Table 1, through the thermodynamic specifications, concluded that hetero-clusters of Ga_8N_9, In_8N_9, $In_4Ga_4N_9$, Si–$In_3Ga_4N_9$, Zn–$In_3Ga_4N_9$ and Ag–$In_3Ga_4N_9$ might be a more efficient structure for energy storage in the solar cells.

Table1. The thermodynamic characters of hetero-clusters of Ga_8N_9, In_8N_9, $In_4Ga_4N_9$, Si–$In_3Ga_4N_9$, Zn–$In_3Ga_4N_9$ and Ag–$In_3Ga_4N_9$ using CAM–B3LYP–D3/6-311+G (d,p) calculation.

Compound	$\Delta E^o_{ads}\times10^{-3}$ (kcal/mol)	$\Delta H^o_{ads}\times10^{-3}$ (kcal/mol)	$\Delta G^o_{ads}\times10^{-3}$ (kcal/mol)	S^o_{ads} (cal/K.mol)	Dipole moment (Debye)
Ga_8N_9	-319.300	-319.299	-319.344	149.170	4.7174
In_8N_9	-318.223	-318.222	-318.266	147.236	6.3277
$In_4Ga_4N_9$	-318.743	-318.743	-318.788	151.994	4.6709
Si–$In_3Ga_4N_9$	-319.979	-319.978	-320.023	150.570	6.2553
Zn–$In_3Ga_4N_9$	-358.610	-358.609	-358.655	151.603	5.9528
Ag–$In_3Ga_4N_9$	-408.962	-408.962	-409.008	154.357	2.9453

Thermodynamic parameters of hetero-clusters of Ga_8N_9, In_8N_9, $In_4Ga_4N_9$, Si–$In_3Ga_4N_9$, Zn–$In_3Ga_4N_9$, and Ag–$In_3Ga_4N_9$ have been assigned through doping of ternary, nanocluster of $In_4Ga_4N_9$ with Si, Zn and Ag towards formation hetero-clusters (Table 1). The changes of Gibbs free energy versus dipole moment could detect the maximum efficiency of Ag–$In_3Ga_4N_9$ hetero-cluster for energy storage in the solar cells through ΔG^o_{ads} (Figure 6).

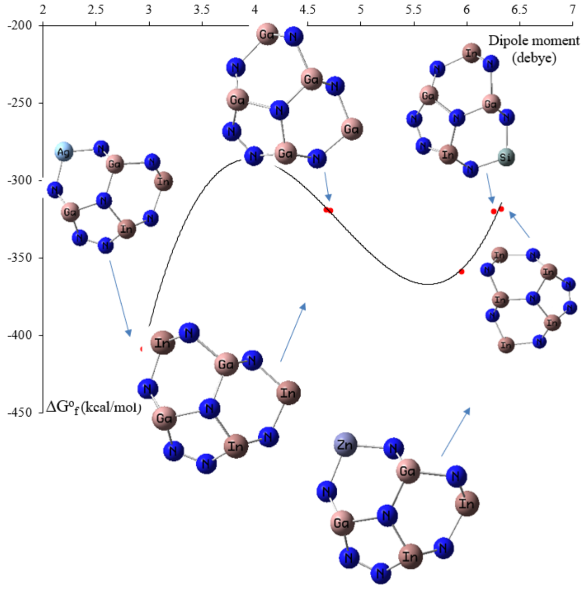

Figure 6. Gibbs free energy (ΔG^o_f) for hetero-clusters of Ga_8N_9, In_8N_9, $In_4Ga_4N_9$, Si–$In_3Ga_4N_9$, Zn–$In_3Ga_4N_9$ and Ag–$In_3Ga_4N_9$.

The adsorption efficiency of Ga_8N_9, In_8N_9, $In_4Ga_4N_9$, Si–$In_3Ga_4N_9$, Zn–$In_3Ga_4N_9$ and Ag–$In_3Ga_4N_9$ based on dipole moment has been evaluated by the ΔG_f^o. The solar cells formed by Ga_8N_9, In_8N_9, $In_4Ga_4N_9$, Si–$In_3Ga_4N_9$, Zn–$In_3Ga_4N_9$ and Ag–$In_3Ga_4N_9$ feature a hierarchical structure with the electron donor/acceptor layer sandwiched by anode and cathode, which raises the importance of controlling the molecular crystal orientation, domain size, and vertical distribution to facilitate the charge collection at electrodes. Doping reduces the composition of indium atoms and the aggregation of In–In and induces deep energy levels. This greatly decreases the defects and improves the valence band potential of $In_3Ga_4N_9$ nanorods. In this paper, we have demonstrated that the ternary semiconductor of Indium Gallium Nitride structure can significantly enhance absorption in a broad spectral range of incident light in the presence of zinc and silver. A comparison between solar cells containing Si-, Zn- or Ag-doped $In_3Ga_4N_9$ shows that the solar cells containing Zn or Ag structures show a more enhanced solar cell performance than the solar cells containing only the single $In_3Ga_4N_9$ structure. This efficient doping strategy bridges the gaps of heteroatom-doped In3Ga4N9-based photoelectrodes and can provide deep insights into controlling the electronic structure for enhanced solar converting yield.

4. Conclusions

In summary, energy grabbing on the hetero-clusters of Ga_8N_9, In_8N_9, $In_4Ga_4N_9$, Si–$In_3Ga_4N_9$, Zn–$In_3Ga_4N_9$, Ag–$In_3Ga_4N_9$ as solar cells was investigated by first-principle calculations. We have provided a ternary semiconductor of Indium Gallium Nitride solar cells doped with silicon, zinc, or silver. The geometrical parameters of doping atoms on the surface of $In_4Ga_4N_9$ through the absorption status and current charge density of the solar cells were studied. Thermodynamic parameters have constructed a detailed molecular model for atom-atom interactions and a distribution of point charges, which can be utilized to reproduce the polarity of the solid material and the adsorbing molecules. Energy storage with hetero-clusters has described that the frame of the overcoming cluster is related to Ag–$In_3Ga_4N_9$ in the high amounts of frequency. This property makes Ag–$In_3Ga_4N_9$ potentially advantageous for certain high-frequency applications requiring solar cells for energy storage. The advantages of silver over indium gallium nitride include its higher electron and hole mobility, allowing silver doping devices to operate at higher frequencies than silicon and zinc doping devices. Thus, it should explore its unique properties, such as its ability to increase energy storage, which could lead to advancements in solar cell systems.

Funding

This research received no external funding.

Acknowledgments

The author is grateful to Kastamonu University for completing this paper and its research.

Conflict of Interest

The author declares no conflict of interest.

References

1. Di Carlo, A. Tuning Optical Properties of GaN-Based Nanostructures by Charge Screening. *Physica Status Solidi A.* **2001**, *183*, 81–85, https://doi.org/10.1002/1521-396X(200101)183:1<81::AID-PSSA81>3.0.CO;2-N.
2. Mollaamin, F.; Monajjemi, M. Determination of GaN nanosensor for scavenging of toxic heavy metal ions (Mn^{2+}, Zn^{2+}, Ag^{+}, Au^{3+}, Al^{3+}, Sn^{2+}) from water: Application of green sustainable materials by molecular modeling approach. *Comput. Theor. Chem*. **2024**, *1237*, 114646. https://doi.org/10.1016/j.comptc.2024.114646
3. J. D. Sun; Y. F. Sun; D. M. Wu; Y. Cai; H. Qin; B. S. Zhang. High-responsivity, low-noise, room-temperature, self-mixing terahertz detector realized using floating antennas on a GaN-based field-effect transistor. *Appl. Phys. Lett.* **2012**, *100*, 013506, https://doi.org/10.1063/1.3673617.
4. Mollaamin, F.; Monajjemi, M. The influence of Sc, V, Cr, Co, Cu, Zn as ferromagnetic semiconductors implanted on B5N10-nanocarrier for enhancing of NO sensing: An environmental eco-friendly investigation. *Comput. Theor. Chem*. **2024**, *1237*, 114666. https://doi.org/10.1016/j.comptc.2024.114666
5. Amano, H.; Kito, M.; Hiramatsu, K.; Akasaki, I. (1989). *P-Type Conduction in Mg-Doped GaN Treated with Low-Energy Electron Beam Irradiation (LEEBI)*. *Japanese Journal of Applied Physics*.**1989**, *28*, L2112, https://doi.org/10.1143/JJAP.28.L2112.
6. Amano, H.; Asahi, T.; Akasaki, I. Stimulated Emission Near Ultraviolet at Room Temperature from a GaN Film Grown on Sapphire by MOVPE Using an AlN Buffer Layer. *Japanese Journal of Applied Physics*. **1990**, *29*, L205, https://doi.org/10.1143/JJAP.29.L205.
7. Akasaki, I.; Amano, H.; Sota, S.; Sakai, H.; Tanaka, T.; Koike, M. Stimulated Emission by Current Injection from an AlGaN/GaN/GaInN Quantum Well Device. Japanese *Journal of Applied Physics.* **1995**, *34*, L1517, https://doi.org/10.7567/JJAP.34.L1517.
8. Kodama, M.; Sugimoto, M.; Hayashi, E.; Soejima, N.; Ishiguro, O.; Kanechika, M.; Itoh, K.; Ueda, H.; Uesugi, T.; Kachi, T. GaN-Based Trench Gate Metal Oxide Semiconductor Field-Effect Transistor Fabricated with Novel Wet Etching. *Appl. Phys. Express* **2008**, *1*, 021104, https://doi.org/10.1143/APEX.1.021104.
9. Wraback, M.; Shen, H.; Carrano, J.C.; Collins, C.J; Campbell, J.C.; Dupuis, R.D.; Schurman, M.J.; Ferguson, I.T. Time-Resolved Electroabsorption Measurement of the electron velocity-field characteristic in GaN. *Applied Physics Letters* **2000**, *76*, 1155-1157, https://doi.org/10.1063/1.125968.
10. Wu, J.; Walukiewicz, W.; Yu, K.M. et al. Superior radiation resistance of $In_{1-x}Ga_xN$ alloys: full-solar-spectrum photovoltaic material system. *J Appl Phys*. **2003**; *94*, 6477-6482, http://dx.doi.org/10.1063/1.1618353.
11. Wu, J.; Walukiewicz, W.; Yu, K. et al. Small band gap bowing in $In_{1-x}Ga_xN$ alloys. *Appl Phys Lett*. **2002**, *80*, 4741-4743, https://doi.org/10.1063/1.1489481.
12. Singh, R.; Doppalapudi, D.; Moustakas, T.D.; Romano, L.T. Phase separation in InGaN thick films and formation of InGaN/GaN double heterostructures in the entire alloy composition. *Appl Phys Lett*. **1997**, *70*, 1089-1091, http://dx.doi.org/10.1063/1.118493.
13. Lie, D.H.; Hsiao, Y.H.; Yang, S.G. et al. Harsh photovoltaics using InGaN/GaN multiple quantum well schemes. *Nano Energy*. **2015**, *11*, 104-109, https://doi.org/10.1016/j.nanoen.2014.10.013.
14. Kuwahara, Y.; Fujii, T.; Fujiyama, Y.; et al. Realization of nitride-based solar cell on freestanding GaN substrate. *Appl Phys Express*. **2010**, *3*, 111001-1-111001-3, https://doi.org/10.1143/APEX.3.111001.
15. Young, N.G.; Farrell, R.M.; Hu, Y.L.; et al. High performance thin quantum barrier InGaN/GaN solar cells on sapphire and bulk (0001) GaN substrates. *Appl Phys Lett*. **2013**; *103*, 173903-1-173903-5, https://doi.org/10.1063/1.4826483.
16. Neufeld, C.J.; Cruz, S.C.; Farrell, R.M.; et al. Effect of doping and polarization on carrier collection in InGaN quantum well solar cells. *Appl Phys Lett*. **2011**, *98*, 243507-1-243507-3, https://doi.org/10.1063/1.3595487.
17. Shen, H.; Maes, B. Combined plasmonic gratings in organic solar cells. *Opt Express*. **2011**, *19*, A1202-A1210, https://doi.org/10.1364/OE.19.0A1202.
18. Wang, K.X.; Yu, Z.; Liu, V.; Cui, Y.; Fan, S. Absorption enhancement in ultrathin crystalline silicon solar cells with antireflection and light-trapping nanocone gratings. *Nano Lett*. **2012**, *12*, 1616-1619, https://doi.org/10.1021/nl204550q.

19. Meng, X.; Drouard, E.; Gomard, G.; Peretti, R.; Fave, A.; Seassal, C. Combined front and back diffraction gratings for broad band light trapping in thin film solar cell. *Opt Express*. **2012**, *20*, A560-A571, https://doi.org/10.1364/OE.20.00A560.
20. Abass, A.; Le, K.Q.; Alu, A.; Burgelman, M.; Maes, B. Dual-interface gratings for broadband absorption enhancement in thin-film solar cells. *Phys Rev B*. **2012**, *85*, 115449-1-115449-8, https://doi.org/10.1103/PhysRevB.85.115449.
21. Chriki R, Yanai A, Shappir J, Levy U. Enhanced efficiency of thin film solar cells using a shifted dual grating plasmonic structure. *Opt Express*. **2013**, *21*, A382-A391, https://doi.org/10.1364/OE.21.00A382.
22. Hsu, W.C.; Tong, J.K.; Branham, M.S.; et al. Mismatched front and back gratings for optimum light trapping in ultra-thin crystalline silicon solar cells. *Opt Commun*. **2016**, *377*, 52-58, https://doi.org/10.1016/j.optcom.2016.04.055.
23. Isabella, O.; Vismara, R.; Ingenito, A.; Rezaei, N.; Zeman, M. Decoupled front/back dielectric textures for flat ultra-thin c-Si solar cells. *Opt Express*. **2016**, *24*, A708-A719, https://doi.org/10.1364/OE.24.00A708.
24. Lin, J.; Yu, Y.; Xu, Z.; Gao, F.; Zhang, Z.; Zeng, F.; Wang, W.; Li, G.; Electronic engineering of transition metal Zn-doped InGaN nanorods arrays for photoelectrochemical water splitting, *Journal of Power Sources* **2020**, *450*, 227578, https://doi.org/10.1016/j.jpowsour.2019.227578.
25. Kumawat, U.K.; Kumar, K.; Bhardwaj, P.; Dhawan, A. Indium-rich InGaN/GaN solar cells with improved performance due to plasmonic and dielectric nanogratings. *Energy Science & Engineering* **2019**, *7*, 2469-2482, https://doi.org/10.1002/ese3.436.
26. Mollaamin, F.; Monajjemi, M. In Silico-DFT Investigation of Nanocluster Alloys of Al-(Mg, Ge, Sn) Coated by Nitrogen Heterocyclic Carbenes as Corrosion Inhibitors. *J Clust Sci* **2023**, *34*, 2901–2918. https://doi.org/10.1007/s10876-023-02436-5
27. Mollaamin, F.; Monajjemi, M. Transition metal (X = Mn, Fe, Co, Ni, Cu, Zn)-doped graphene as gas sensor for CO_2 and NO_2 detection: a molecular modeling framework by DFT perspective. *J Mol Model* **2023**, *29*, 119. https://doi.org/10.1007/s00894-023-05526-3
28. Mollaamin, F.; Shahriari, S.; Monajjemi, M. et al. Nanocluster of Aluminum Lattice via Organic Inhibitors Coating: A Study of Freundlich Adsorption. *J Clust Sci* **2023**, *34*, 1547–1562. https://doi.org/10.1007/s10876-022-02335-1
29. Mollaamin,F.; Monajjemi,M. Trapping of toxic heavy metals from water by GN–nanocage: Application of nanomaterials for contaminant removal technique. *J. Mol. Struct*. **2024**, *1300*, 137214. https://doi.org/10.1016/j.molstruc.2023.137214
30. Mollaamin, F. Competitive Intracellular Hydrogen-Nanocarrier Among Aluminum, Carbon, or Silicon Implantation: a Novel Technology of Eco-Friendly Energy Storage using Research Density Functional Theory. *Russ. J. Phys. Chem. B* **2024**, *18*, 805–820. https://doi.org/10.1134/S1990793124700131
31. Mollaamin, F.; Monajjemi, M. Tailoring and functionalizing the graphitic-like GaN and GaP nanostructures as selective sensors for NO, NO_2, and NH_3 adsorbing: a DFT study. *J Mol Model* **2023**, *29*, 170. https://doi.org/10.1007/s00894-023-05567-8
32. Monajjemi, M.; Mollaamin, F. Development of Solid-State Lithium-Ion Batteries (LIBs) to Increase Ionic Conductivity through Interactions between Solid Electrolytes and Anode and Cathode Electrodes. *Energies* **2024**, *17*, 4530. https://doi.org/10.3390/en17184530
33. Mollaamin, F.; Monajjemi, M. Doping of Graphene Nanostructure with Iron, Nickel and Zinc as Selective Detector for the Toxic Gas Removal: A Density Functional Theory Study. *C–Journal of Carbon Research* **2023**, *9*, 20. https://doi.org/10.3390/c9010020
34. Zadeh, M.A.A.; Lari, H.; Kharghanian, L. et al. Density Functional Theory Study and Anti-Cancer Properties of Shyshaq Plant: In View Point of Nano Biotechnology. *J. Comput. Theor. Nanosci*. **2015**, *12*, 4358. https://doi.org/10.1166/jctn.2015.4366
35. Mollaamin, F.; Monajjemi, M. Application of DFT and TD-DFT on Langmuir Adsorption of Nitrogen and Sulfur Heterocycle Dopants on an Aluminum Surface Decorated with Magnesium and Silicon. *Computation* **2023**, *11*, 108. https://doi.org/10.3390/computation11060108
36. Bakhshi, K.; Mollaamin, F.; Monajjemi, M. Exchange and Correlation Effect of Hydrogen Chemisorption on Nano V(100) Surface: A DFT Study by Generalized Gradient Approximation (GGA). *J. Comput. Theor. Nanosci*. **2011**, *8*, 763–768. https://doi.org/10.1166/jctn.2011.1750
37. Mollaamin, F.; Monajjemi, M. Adsorption ability of Ga_5N_{10} nanomaterial for removing metal ions contamination from drinking water by DFT. *Int. J. Quantum Chem*. **2024**, *124*, e27348, https://doi.org/10.1002/qua.27348.

38. Mollaamin, F.; and Monajjemi M. Molecular modelling framework of metal-organic clusters for conserving surfaces: Langmuir sorption through the TD-DFT/ONIOM approach. *Molecular Simulation* **2023**, *49*, 365–376. https://doi.org/10.1080/08927022.2022.2159996.
39. Mollaamin, F.; Monajjemi, M. Nanomaterials for Sustainable Energy in Hydrogen-Fuel Cell: Functionalization and Characterization of Carbon Nano-Semiconductors with Silicon, Germanium, Tin or Lead through Density Functional Theory Study. *Russ. J. Phys. Chem. B* **2024**, *18*, 607–623. https://doi.org/10.1134/S1990793124020271
40. Frisch, M. J.; Trucks, G. W.; Schlegel, H. B.; Scuseria, G. E.; Robb, M. A.; et al. Gaussian 16, Revision C.01, Gaussian, Inc., Wallingford CT, **2016**.
41. GaussView, Version 6.06.16, Dennington, Roy; Keith, Todd A.; Millam, John M. Semichem Inc., Shawnee Mission, KS, **2016**.
42. Xu, Z.; Qin, C.; Yu, Y.; Jiang, G.; Zhao, L. First-principles study of adsorption, dissociation, and diffusion of hydrogen on α-U (110) surface. *AIP Advances* **2024**, *14*, 055114, https://doi.org/10.1063/5.0208082.
43. O'Boyle, N.M.; Tenderholt, A.L.; Langner, K.M. Cclib: A Library for Package-Independent Computational Chemistry Algorithms. *J. Comp. Chem.* **2008**, *29*, 839-845, http://dx.doi.org/10.1002/jcc.20823.
44. Steinmann, S.N.; Mob, Y. Corminboeuf, C. How do electron localization functions describe π-electron delocalization?. *Phys. Chem. Chem. Phys*. **2011**, *13*, 20584-20592, https://doi.org/10.1039/C1CP21055F.
45. Becke, A. D. Edgecombe, K. E. A simple measure of electron localization in atomic and molecular systems, *J. Chem. Phys.* **1990**, *9*, 5397–5403, https://doi.org/10.1063/1.458517.
46. Tian, L.; Feiwu, C.; Xuebao, W. Meaning and Functional Form of the Electron Localization Function. *Acta Phys. Chim. Sin*. **2011**, *27*, 2786–2792, https://doi.org/10.3866/PKU.WHXB20112786.
47. Savin, A.; Jepsen, O.; Flad, J.; Andersen, O.K.; Preuss, H.; von Schnering, H. G. Electron Localization in Solid-State Structures of the Elements: the Diamond Structure, Angew. *Chem. Int. Edit. Engl.* **1992**, *31*, 187, https://doi.org/10.1002/anie.199201871.
48. Trontelj, Z.; Pirnat, J.; Jazbinšek, V.; Lužnik, J.; Srčič, S.; Lavrič, Z.; Beguš, S.; Apih, T.; Žagar, V.; Seliger, J. Nuclear Quadrupole Resonance (NQR)—A Useful Spectroscopic Tool in Pharmacy for the Study of Polymorphism. *Crystals* **2020**, *10*, 450, https://doi.org/10.3390/cryst10060450.
49. Sciotto, R.; Ruiz Alvarado, I.A.; Schmidt, W.G. Substrate Doping and Defect Influence on P-Rich InP(001):H Surface Properties. *Surfaces* **2024**, *7*, 79-87, https://doi.org/10.3390/surfaces7010006.
50. Luo, J.; Wang, C.; Wang, Z.; Guo, Q.; Yang, J.; Rui Zhou, R.; Matano, K.; Oguchi, T.; Ren, Z. NMR and NQR studies on transition-metal arsenide superconductors LaRu2As2, KCa2Fe4As4F2, and A2Cr3As3*. *Chinese Physm* **2020**, *B29*, 067402, https://doi.org/10.1088/1674-1056/ab892d.
51. Young, H.D.; Freedman, R.A.; Ford, A.L. Sears and Zemansky's University Physics with Modern Physics, 13th Edition, Addison-Wesley: **2011**; pp. 754.
52. Sohail, U.; Ullah, F.; Binti Zainal Arfan, N.H.; Abdul Hamid, M.H.S.; Mahmood, T.; Sheikh, N.S.; Ayub, K. Transition Metal Sensing with Nitrogenated Holey Graphene: A First-Principles Investigation. *Molecules* **2023**, *28*, 4060, https://doi.org/10.3390/molecules28104060.